Int J Adv Manuf Technol (2016) 87:2041–2061
DOI 10.1007/s00170-016-8563-y

ORIGINAL ARTICLE

Assessment of cutting forces and hole quality in drilling Al2024 aluminium alloy: experimental and finite element study

Khaled Giasin[1] · **Alma Hodzic**[1] · **Vaibhav Phadnis**[1] · **Sabino Ayvar-Soberanis**[1]

Received: 10 September 2015 / Accepted: 29 February 2016 / Published online: 17 March 2016

Abstract Machining experiments were conducted to evaluate the impact of cutting parameters on the hole quality and cutting forces in drilling Al2024-T3 aerospace alloy. Al2024-T3 specimen were drilled using Φ6-mm TiAlN-coated carbide twist drills under dry cutting conditions. The hole quality was inspected in terms of its surface roughness, burr and chip formations, hole size, circularity error and post-machining microhardness of the subsurface of the holes. An analysis of variance (ANOVA) was carried out to determine the percentage contribution of cutting parameters on cutting forces and the inspected hole quality parameters. A three-dimensional (3D) finite element (FE) model of drilling Al2024-T3 is developed using Abaqus/Explicit to predict thrust force and torque. The FE model was validated using experimental results and found to be in good agreement. The results of the study showed that the cutting parameters have a significant impact on cutting forces and inspected hole quality parameters. Drilling at feed rates of 100 and 300 mm/min and spindle speeds of 1000, 3000, and 6000 rpm are recommended for producing holes with smaller surface roughness, deviation from nominal hole size, circularity error and burrs.

Keywords Drilling · Al2024 · Burr formation · Surface roughness · Hardness · Finite element analysis

✉ Khaled Giasin
meq11kg@sheffield.ac.uk

[1] The University of Sheffield, Sheffield, UK

1 Introduction

Aluminium and its alloys are one of the key materials used in automotive and aerospace applications. Drilling accounts for about 40 % of the total material removal process in automotive industries [1]. The use of Al2024-T3 can be found in fuselage skin and wing sections of the aircraft [2] due to its high specific strength, stiffness and excellent corrosion resistance. A typical commercial aircraft often requires drilling numerous holes for assembly purpose; for example, it is estimated that nearly 2000 holes are drilled into flap skins to attach them to the frame of the aircraft [3]. Most of the previous studies on machining Al2024-T3 alloy focused on turning, orthogonal cutting and milling operations [4–14], whilst fewer studies were reported on drilling Al2024-T3 [2, 5, 15–23] as shown in Table 1.

The selection of cutting speeds and feed rates depends on the mechanical properties of the workpiece, the type of material used for the drill bit and its coating. Koklu et al. [18] previously reported that the mechanical properties of drilled aluminium alloy can influence the burr height and surface roughness, such that the higher the ductility of the alloy, the greater is the amount of burr formed around the drilled hole. In addition, the surface roughness increases with the increase of cutting parameters and drill size [18, 21]. Most Al2024 drilling studies used a tool diameter between 5 and 10 mm since it is a common range for creating rivets and hole in aerospace alloys (see Table 1). Previous findings also showed that effect of feed rate was more dominant on cutting forces, burr formations and tool life [18, 23]. In addition, HSS cutting tools were found unsuitable for drilling aluminium alloys such as Al2024-T3 especially in dry drilling process [15]. Whilst coated carbide tools such as TiAlN coating have excellent wear and oxidation resistance and is suitable for in dry machining applications of alloyed steel and aluminium alloys with 10 %

Table 1 Summary of most recent studies on drilling Al2024-T3 alloy

Al alloy	Drill size/coating	Cutting parameters	Objectives	Ref
Al2024-T351	6-mm HSS carbide uncoated and multilayer TiAlN, TiAlN/WC + C, TiN, Tin + Ag coated drills 130°, 140° point angle, 10°, 30°, 40° helix angle	1361, 8754 rpm 0.04 mm/rev	G W R Z	[5, 15]
Al2024-T3	4.76 -mm HSS drill, 118° point angle	Not specified	R W	[2]
Al2024	10 mm HSS uncoated and HSS + TiALN, HSS + TiN, TiAlN, TiN, % Co 118°, 130° point angle, 24°, 30° helix angle	955, 1432, 1910 rpm 0.15, 0.2, 0.25 mm/rev	R Z Y	[16, 17]
Al-2024	8, 10, 12-mm uncoated HSS drills	796–1592 rpm 0.05, 0.1, 0.15	R B	[18]
Al2024	6-mm HSS and HSS cobalt drills 130° point angle, 30°, 40° helix angle	1500, 5000 rpm 0.04 mm/rev	W Z C	[19]
Al2024-T6 vibrational drilling	5-mm HSS drill, 118° point angle	460, 750, 1255 rpm 0.104, 0.208, 0.348 mm/rev	C B F	[20]
Al2024	6-mm HSS drill bit	609, 833, 1183 rpm 0.31, 0.68, 0.8 mm/min	R Z	[21]
Al2024-T6 vibrational drilling	5-mm HSS twist drill, 118° point angle	460, 755, 1255 rpm 0.104, 0.208, 0.348 mm/rev	V C F R	[22]
Al2024-T351	6.35-mm CVD diamond 120° point angle, 34° helix angle	2506, 5013, 7519 rpm 0.08, 0.16, 0.24 mm/rev	B Z E	[23]

B burr formation, *C* cutting forces, *E* roundness, *F* chip formation, *G* coating performance, *R* surface roughness, *U* ultrasonic vibrations, *W* tool wear, *Y* circularity, *Z* hole size

content of silicon due to its low thermal conductivity [5], Davoudinejad et al. [19] reported that the use of high cutting speeds for drilling Al2024-T3 increased the deviation of hole size and the built-up edge (BUE) formed on the chisel edge and cutting lips, which in return increased the cutting forces.

Amini et al. [20] and Barani et al. [24] reported that vibrational drilling of Al2024-T6 alloy could help reduce cutting forces by up to 70 % compared to conventional drilling, in addition reduce exit burr formations and increase chip breakability which reduced built edge and dimensional deviation of hole size. The recommended point angles for drilling aluminium alloys with low or no silicon content range between 130° and 140° and between 115° and 120° for high silicon content aluminium alloys [25]. Nouari et al. [5] reported that the surface roughness is affected by the point and helix angles, such that increasing these two parameters can minimise roughness. In addition, a larger point angle will minimise burr height [5, 26], whilst a larger helix angle will give minimum diameter deviation compared to the nominal hole diameter which gives good dimensional accuracy [5].

Since large amounts of chips are created during the machining of aluminium, chip morphology and its characteristics were the focus of several studies [27, 28]. These studies looked into the effect of cutting parameters, tool geometry

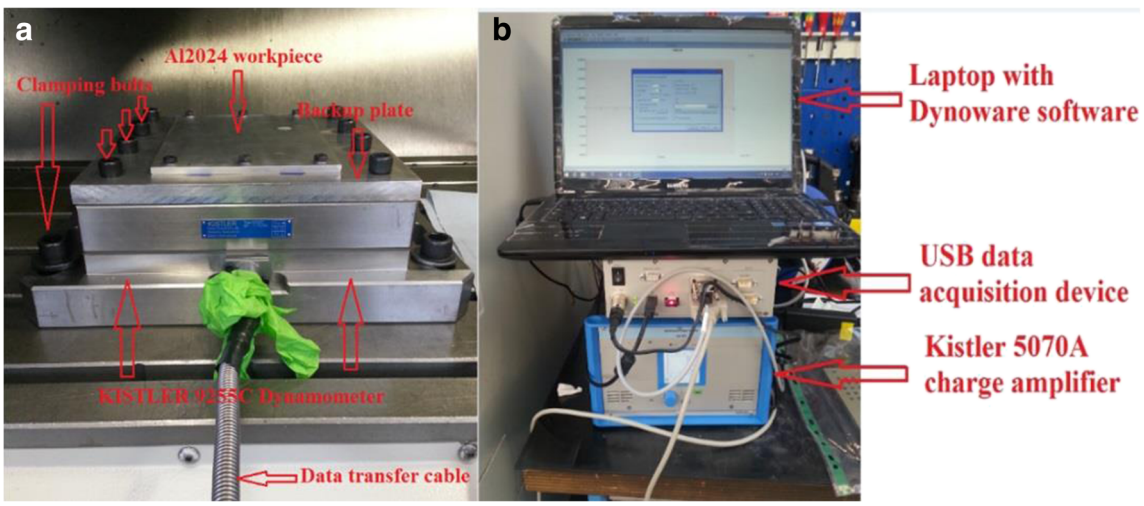

Fig. 1 **a** Workpiece and dynamometer setup inside the CNC machine **b** Data acquisition setup of cutting forces

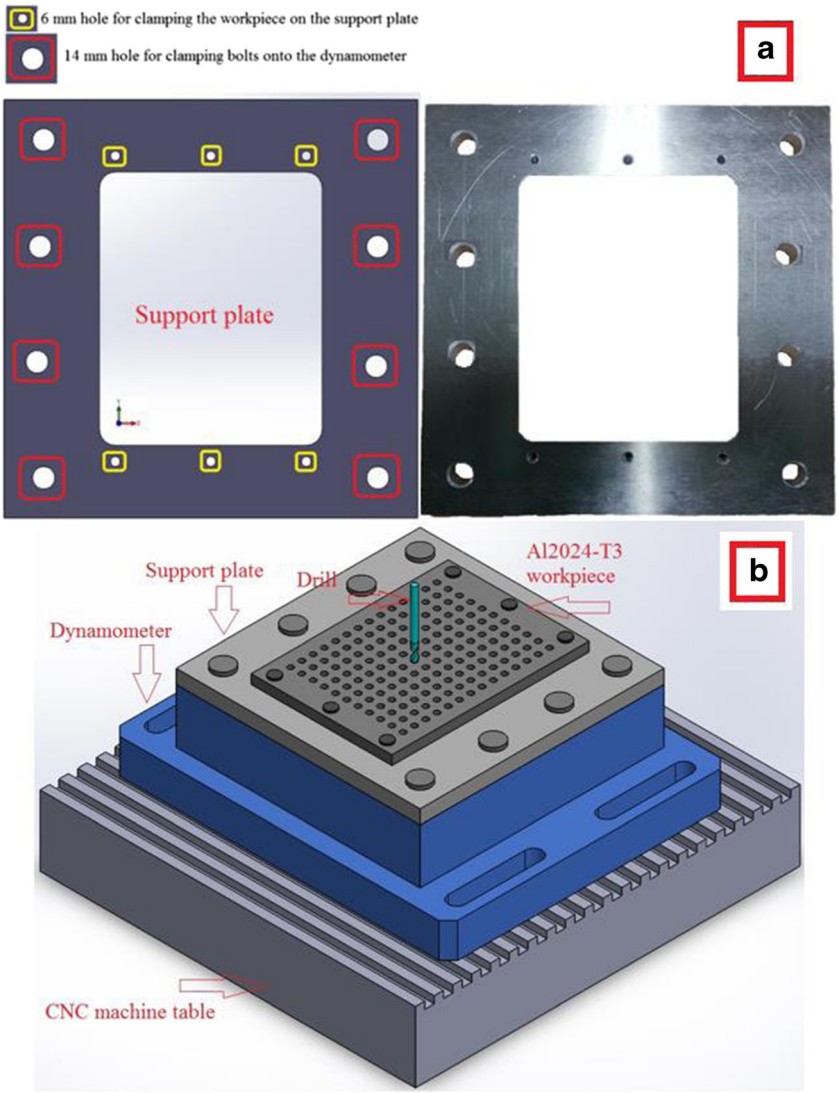

Fig. 2 Hollow support plate and **b** dynamometer/workpiece setup inside the CNC machine

and their coating on chip formation and morphology. Results showed that chip size and length vary with cutting parameters and tool geometry, besides the effect of coolants that was considered to be an important factor in controlling chip formation and evacuation.

The investigation of any machining study requires extensive experimental trials in order to reach to optimum design; this would turn to be costly and time-consuming. Finite element (FE) analysis can provide a comprehensive analysis of machining operations to accurately replicate the performance of the actual machining process, which allows for cost-effective product development and overcomes design problems prior actual machining.

The FE analysis of metal machining that have been the aim of many researchers in their previous studies in order to predict the characteristics of machining operations is a useful tool to minimise the costs of materials and maximise productivity. 2D and 3D FE models were developed to simulate the machining process in order to predict the cutting forces [12, 29–31], tool and workpiece temperatures [12, 31, 32], chip morphology [31, 33–36], residual stresses [37] and friction coefficient [38] of various metals with

Table 2 Chemical composition (wt%) of Al2024-T3 [19]

Component	Aluminium	Chromium	Copper	Iron	Magnesium	Manganese	Silicon	Titanium	Zinc
Percentage (%)	90.7–94.7	0.1	3.4–4.9	0.5	1.2–1.8	0.3–0.9	0.5	0.25	0.25

Table 3 Spindle speeds and feed rates used in the experiments

Levels	Level 1	Level 2	Level 3	Level 4
Spindle speed (rpm)	1000	3000	6000	9000
Feed rate (mm/min)	100	300	600	900

extensive focus on some metals such as steel, aluminium, titanium and Inconel.

The aim of the work is to extend the fundamental knowledge when machining Al2024-T3 aluminium alloy through the assessment of twist drilling operations in order to improve productivity and workpiece quality. The work is carried out by investigating the influence of cutting parameters on hole quality when drilling Al2024-T3 aerospace alloy. The analysed hole parameters are some of the most critical factors which determine the surface integrity of machined aerospace structures, besides the investigation into the feasibility of finite element modelling of the drilling process of Al2024-T3 alloy to predict the cutting forces as a useful tool in machining applications.

2 Experiments

2.1 Machine setup

The drilling experiments were conducted using MORI-SEIKI SV-500 CNC milling machine. The machine is capable of providing spindle speeds up to 10,000 rpm. Thrust force (F_z) and torque (M_z) were recorded during the drilling process using a piezoelectric multicomponent dynamometer (KISTLER 9255C). An eight-channel charge amplifier type 5070A was connected to a USB data acquisition system (type 5697A); the recorded data were analysed using Dynoware software as shown in Fig. 1.

The Al2024-T3 workpiece was bolted to the hollow support plate as shown in Fig. 2a. This assembly was then mounted on the top of the dynamometer (see Fig. 2b). The main purpose of the support plate is to protect the dynamometer during the drilling process and to allow for chip evacuation from the drill exit side. The cutting forces F_x, F_y, and F_z were calculated directly during the drilling process. The torque was also calculated using type 1.a (eight-channel) option, which is a multicomponent mode with the KISTLER 9255C stationary dynamometer. The torque M_z was calculated by inputting the distance to the centre of each hole from the centre point of each of the four piezoelectric sensors in the dyno. The datum coordinates are inserted in Dynoware software prior the drilling of each hole to calculate the torque during the drilling process.

2.2 Drilling trials

The cutting tool considered in this work was OSG HYP-HP-3D Φ6-mm TiAlN-coated carbide twist drill with a point angle of 140°, a helix angle of 30° and total length of 66 mm. The Al2024-T3 sample used measures 150 × 200 × 7.1304. The chemical composition of Al2024-T3 used is shown in Table 2.

This experiment combined four spindle speeds and four feed rates (four-level full factorial design). In order to confirm the repeatability of the experiment, each drilling trial was repeated three times and mean values of the average forces were reported. All results reported here were average data of three repetitions with error bars representing twice the standard deviation (STD) of the measured parameter. Two holes were

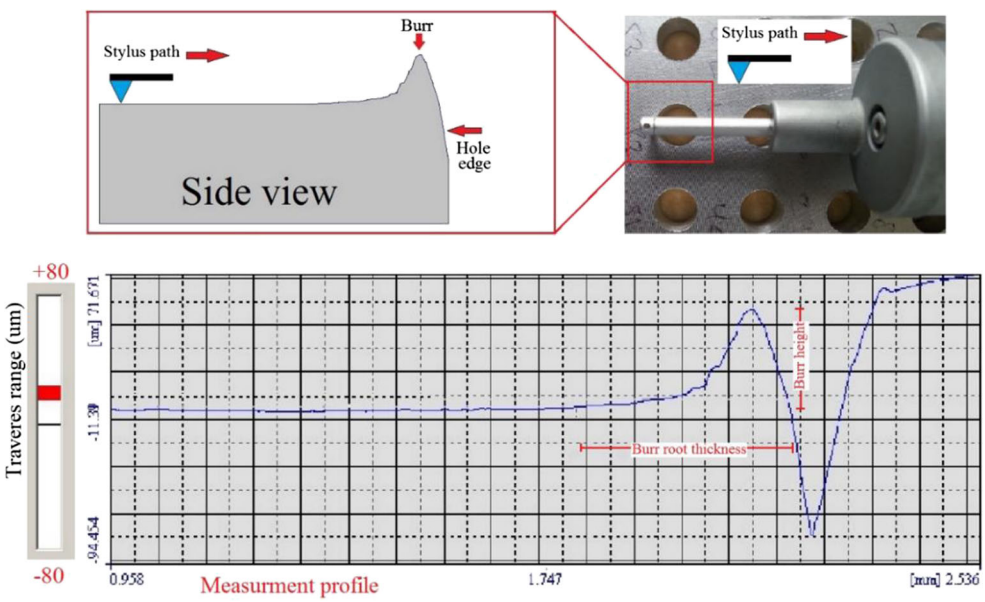

Fig. 3 Measurement of burr height and root thickness

drilled at high feed rates (600 and 900 mm/min) and low spindle speed (1000 rpm) to generate the ANOVA tables and to evaluate the effect of excessive feeding on hole quality. Each set of 16 holes was drilled with a new tool to minimise any effect of tool wear, adhesions or BUE; no coolants were used in this study. Table 3 summarises the cutting parameters used in the experiment:

2.3 Analysis of hole quality and tool condition

2.3.1 Measuring burr formations

The quality of drilled holes was inspected in terms of burr formation which included measuring the burr height and burr root thickness at the entrance and the exit side of each drilled hole. Burrs were measured using Mitutoyo SV-602 profilometer at 0, 90, 180, and 270° around the hole, and their average was taken for the final burr value, as shown in Fig. 3. The stylus was placed few millimetres away from the hole edge at the stated locations (0, 90, 180, and 270° around the hole) and is then allowed to move towards the centre of the hole. The stylus records the changes in the surface height of the path it is moving on whilst in motion. The software is programmed to trace (plot) the measured profile and stop the stylus movement if the height measured by the stylus exceeds the traverse range of the profilometer (two traverse range options are available, either ±300 or ±80 μm); the latter option was chosen. The stylus exceeds those limits when it reaches the edge of the hole after it has passed over the burr as shown below (see Fig. 4). The path of the stylus profile is plotted in the software, and the measurement tools in the software are used to calculate the burr height and the burr root thickness.

2.3.2 Measuring surface roughness

The hole average surface roughness R_a was also measured using Mitutoyo SV-602 roughness device at 0, 90, 180, and 270° around the hole wall by rotating the sample along its edges as shown in Fig. 4, and their average was taken as the final surface roughness value R_a.

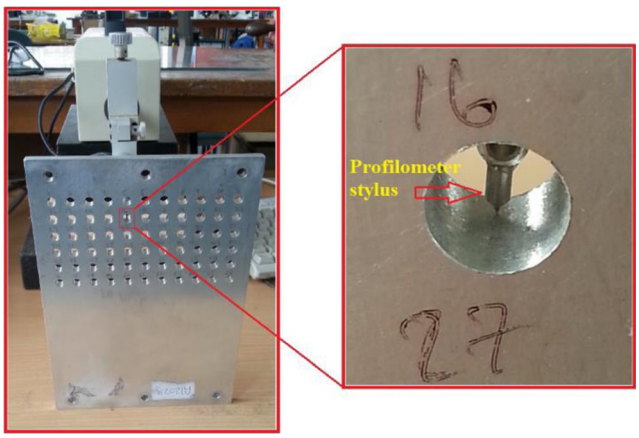

Fig. 4 Measurement of the average surface roughness R_a

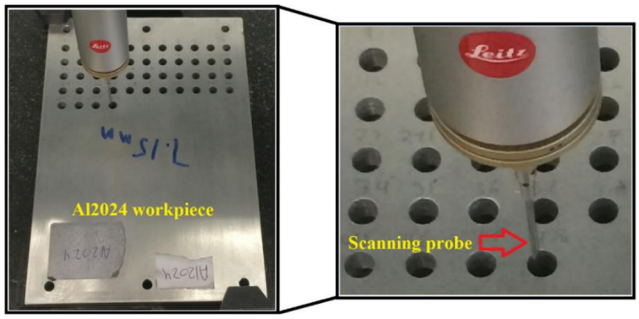

Fig. 5 Measurement of hole size and circularity error

2.3.3 Measuring hole size and circularity error

Hole size and circularity error were measured to inspect the deviation from the nominal diameter. Both parameters were measured using SHEFFIELD CORDAX D8 CMM machine using a 2-mm ruby probe as shown in Fig. 5. The measurements were carried out at two, 1 and 6 mm, depths beneath the upper surface of the hole, and they were referred to in the paper hereafter as top and bottom locations. The scanning speed for the probe was 1 mm per second, which allowed it to capture 400 points whilst scanning around the borehole surface.

2.3.4 Measuring the post-machining microhardness

The Vickers microhardness of the entrance and exit surface of the hole were measured to evaluate the post-machining hardness change in the workpiece. The measurement was taken near the hole edge using Mitutoyo HM-101 Vickers microhardness testing machine using diamond indenter applied with 1000-gf load and 15-s dwell time as shown in Fig. 6. The cutting tools and collected chips were inspected under optical microscopy to determine the influence of cutting parameters

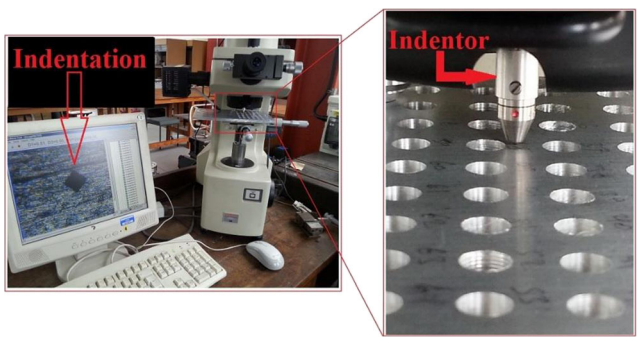

Fig. 6 Measurement of post-machining microhardness

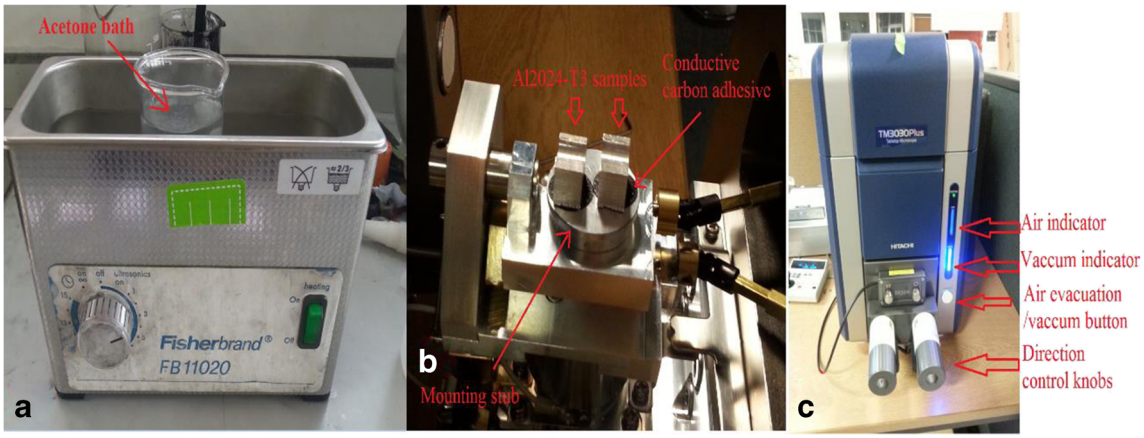

Fig. 7 **a** SEM sample preparation, **b** Al2024 samples mounted inside the SEM chamber, and **c** Hitachi TM3030 tabletop SEM microscope

on chip formation and to assess the tool condition after the end of the machining process.

2.3.5 Scanning electron microscopy

The scanning electron microscopy (SEM) technique was employed to analyse drilling-induced damage to the bore wall surface. Each hole was cross sectioned from its centre and undergone ultrasonic cleaning process in an acetone bath for 10 min to remove dust and debris from the inner surface of the borehole as shown in Fig. 7a. The samples were then placed on the top of a carbon sticker and inserted inside the SEM chamber for surface inspection as shown in Fig. 7b, c. The SEM scanning was conducted using Hitachi HM3030 plus tabletop microscope.

3 Experimental results

3.1 Cutting force analysis

Figure 8 shows the schematic of the thrust force and torque, respectively, when drilling a hole using the cutting speed of $n = 3000$ rpm and feed rate of $f = 900$ mm/min. The drilling process can be clearly divided into three stages according the chisel edge position with respect to the workpiece. Initially, the cutting tool is not in contact with the workpiece and no forces are recorded. Next, the cutting tool advances into the workpiece and a sharp increase in cutting forces due to drill-workpiece contact starts to accumulate (entry stage). At this stage, the chisel edge of the cutting tool is not entirely inside the workpiece, the increase in cutting force continues until the cutting tool chisel edges fully engage with the workpiece and thrust force and torque profiles remain almost constant at which maximum cutting forces are observed. The fluctuations were found to increase with spindle speed. Once the cutting tool reaches the end of the workpiece, the thrust force and torque drop down sharply (exit stage) similar to the entry stage indicating the end of hole drilling.

Figures 9 and 10 show the influence of feed rate and spindle speed on thrust force and torque when drilling Al2024-T3 workpiece. Results show that cutting forces increased with the increase of the feed rate and decreased with the increase of the spindle speed. The influence of the spindle speed on cutting forces was more dominant than the feed rate. The lowest thrust force was observed when drilling at a feed rate of $f = 100$ mm/min and spindle speed of $n = 9000$ rpm; the highest was obtained at $f = 900$ mm/min and 1000 rpm. Whilst the lowest torque occurred when drilling at feed rate of $f = 100$ mm/min and spindle speed of $n = 6000$ rpm, which indicates that

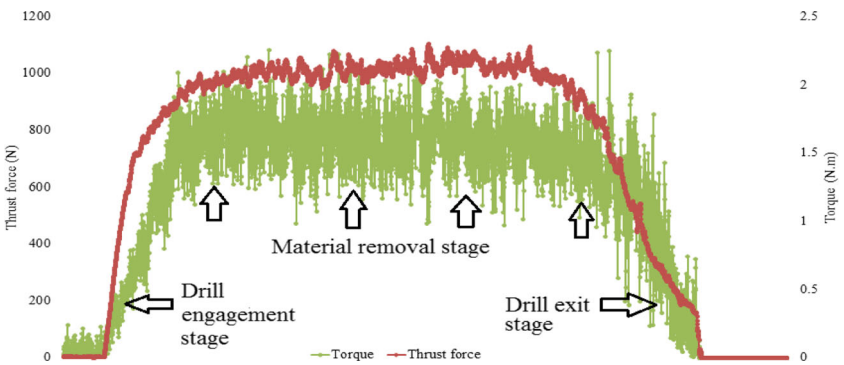

Fig. 8 Thrust force and torque profiles in drilling Al2024-T3 ($n = 3000$ rpm and $f = 900$ mm/min)

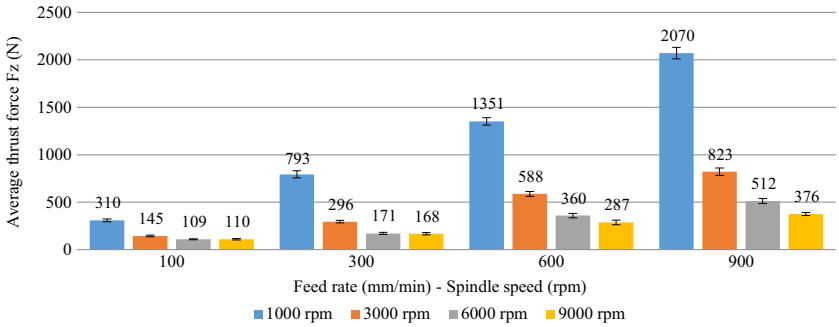

Fig. 9 Average thrust force under different cutting conditions

excessive spindle speed might increase the torque due to increased friction and vibrations of the drill, the highest torque was obtained at $f = 900$ mm/min and 1000 rpm.

It was also observed that when drilling at feed rate and spindle speed combinations of 0.1 mm/rev (100/1000, 300/3000, 600/6000 and 900/9000), thrust force reduced by 4.7 % when drilling at $f = 300$ mm/min compared with drilling at $f = 100$ mm/min and by 21–22 % compared with drilling at $f = 600$ and 900 mm/min, respectively. In addition, drilling at $f = 300$ and 600 mm/min reduced torque by 14.5–15.5 % than at $f = 100$ mm/min and by 21–22 % than at $f = 900$ mm/min; this might indicate that increasing the cutting parameters would results in higher cutting forces.

Table 4 summarises the percentage contribution of spindle speed, feed rate and their interaction on the cutting forces and hole quality parameters. For thrust force, results showed that spindle speed had the highest contribution of 48.36 %, followed by feed rate with 32.03 %; the interaction of cutting parameters had a small effect of about 19.40 %. Similarly, for the torque, the spindle speed was more dominant with 50.84 %, whilst the contribution of the feed rate was 29.30 and 17.86 % for their interaction.

3.2 Hole quality analysis

3.2.1 Surface roughness

Figure 11 shows the average surface roughness R_a of drilled holes under different cutting conditions; the surface roughness ranged between 1.159 and 7.96 μm, and the lowest R_a was measured for a hole drilled at $n = 3000$ rpm and $f = 600$ mm/min and highest at $n = 1000$ rpm and $n = 900$ mm/min. Generally, surface roughness increased with the increase of spindle speed and feed rate. The continuous rubbing of the cutting tool on the drilled hole walls heats up the tool and the workpiece which increases the ductility and deformations of drilled hole, leading to higher surface roughness.

The influence of feed rate varied at different cutting conditions; for $n = 1000$ and $n = 9000$ rpm, the surface roughness increased with the increase of the feed rate, whilst it decreased with its increase at $n = 3000$ and $n = 6000$ rpm with exception at $f = 900$ mm/min. The influence of spindle speed on surface roughness was greater than that of the feed rate as shown previously in ANOVA (Table 3). The contribution of spindle speed was around 19.97 % whilst feed rate influence was 30.19 %, whilst their interaction had a significant contribution of 47.67 %. It was also observed that when drilling at feed rates/spindle speed ratios of 0.1 mm/rev, the surface roughness increased—despite reducing the machining time, which indicates that increasing the cutting speed would compromise the surface quality of the hole.

3.2.2 Burr formation

Figures 12 and 13 show the average burr height and burr root thickness at hole entry and exit sides under different cutting parameters. Results show that both burr parameters increased with the increase of the feed rate and decreased with the

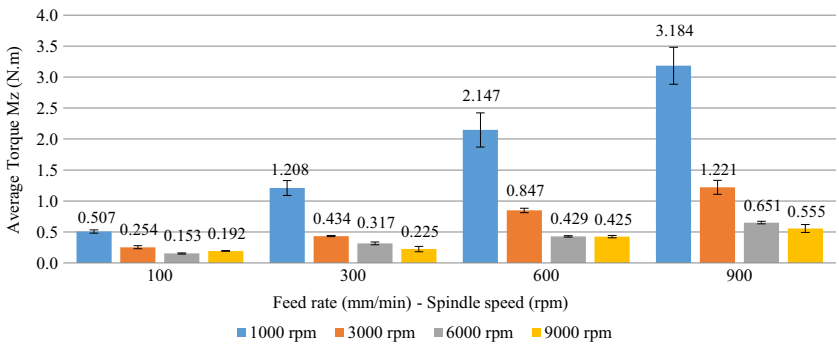

Fig. 10 Average torque under different cutting conditions

Table 4 Percentage contribution of cutting parameters on analysed factors using ANOVA

	Percentage contribution (%)			
	Spindle speed	Feed rate	Spindle speed × feed rate	Error
Thrust force	48.36	32.03	19.40	0.18
Torque	50.84	29.30	17.86	1.98
Surface roughness	19.97	30.19	47.67	2.15
Bur height at entrance	25.83	31.84	21.65	20.67
Burr height at exit	26.89	33.15	29.83	10.11
Burr root thickness at entrance	22.43	21.70	17.17	38.68
Burr root thickness at exit	41.412	33.641	20.841	4.106
Hole size at top	Insignificant	Insignificant	Insignificant	63.285
Hole size at bottom	Insignificant	Insignificant	Insignificant	72.493
Hole circularity at top	Insignificant	Insignificant	Insignificant	49.858
Hole circularity at bottom	Insignificant	Insignificant	Insignificant	68.087

increase of spindle speed when drilling at $n = 1000$, 3000 and 6000 rpm, whilst it increased with it at $n = 9000$ rpm. This could due to the fact that burr height greatly depends on the ductility of the material, such that the higher the ductility, the greater the burr height [39]. In addition, increasing the spindle speed increases the temperatures at the interface between the tool and the workpiece, which increase the plastic deformation of the Al alloy and therefore, increasing the burr height [40].

The feed rate was more dominant on the average burr height on both sides than the spindle speed (see Table 4). The contribution of spindle speed on burr height ranged between 25.83 and 26.896 % and between 22.43 and 44.41 % for burr root thickness. The feed rate contribution on burr height ranged between 31.84 and 31.15 % and between 21.707 and 33.64 % for burr root thickness. The interaction of both cutting parameters seemed to have a significant influence, which ranges from 1717 to 20.84 % for both burr parameters. The impact of spindle speed, feed rate and their interaction becomes more significant at the exit side of the hole due to the increased ductility and deformations with depth, which increases burr formations considerably.

Burr height at exit side was two to three times greater than at entrance side as it can be seen from Fig. 14. Results also showed that drilling at high spindle speed and low feed rates produced smaller burrs on both sides, which could indicate that burr formation can be minimised when drilling under those conditions. Al2024-T3 alloy have a relatively high percentage of elongation; this directly affects the burr formation since the amount of plastic deformation is governed by the ductility of the material and its elongation [18]. Therefore, higher spindle speeds and feed rates can cause higher burr formation. The smallest burr height at hole entrance was achieved when drilling at $n = 6000$ rpm and $f = 3000$ mm/min, whereas the smallest burr height at exit was achieved when drilling at $n = 3000$ rpm and $f = 1000$ mm/min.

3.2.3 Hole size and circularity error

Figures 15 and 16 show the average hole diameter (size) and their circularities, respectively, under different cutting parameters. Oversized holes were produced at both measured locations, and similar results were reported by Abdelhafeez et al. [23]. The hole oversize at the top was greater than at bottom at $f = 300$ and 600 mm/min and $n = 3000$, 6000, and 9000 rpm, which could suggest the possibility of drill 'wander' on contact with the workpiece [23]. The top hole size decreased with

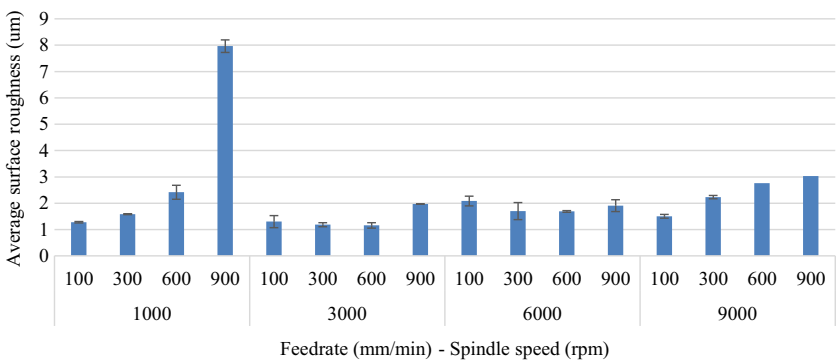

Fig. 11 Average surface roughness

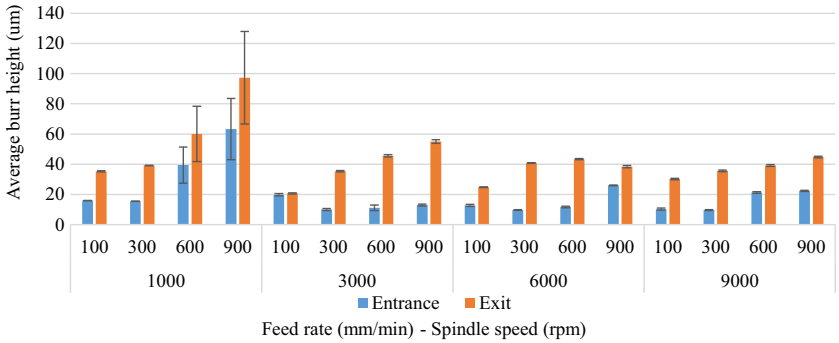

Fig. 12 Average burr height at entrance and exit

feed rates of $f = 100$, 300 and 600 mm/min at $n = 1000$ and 3000 rpm and increased with it from $f = 100$ to 900 mm/min at $n = 6000$ and 9000 rpm. The bottom hole oversize generally decreased with feed rate when drilling at $f = 100$, 300 and 600 mm/min and increased thereafter. This indicates that excessive spindle speed or feed rate might cause the hole to deviate from its nominal diameter, which could be due to the fact that aluminium alloys are difficult to machine under dry conditions due to their high thermal expansion coefficient compared to other metals. The continuous rubbing of the tool on the wall of the hole being drilled can lead to accumulation of hot chips and the expansion of tool and the workpiece creating thermal distortions that influence the accuracy of the machined hole [41]. The hole oversize ranged between 0.712 and 40.32 μm. The minimum deviation in hole size was achieved when drilling at $n = 3000$ rpm and $f = 600$ mm/min. The analysis of ANOVA revealed that cutting parameters and their interactions were insignificant for hole size and circularity at the entrance, which was also reported by Abdelhafeez et al. [23].

The error from the ANOVA analysis was high for both the hole size and circularity error, which indicates that the model is not capable of detecting the contribution of the cutting parameters and higher-order models should be implemented to further analyse the results which will be carried out in a future work. The circularity error at top increased with feed rate when drilling at $n = 3000$, whilst it decreased with feed rates of $n = 1000$ and 9000 rpm. At bottom, the circularity error increased with feed rates of $n = 3000$ and 6000 rpm, whilst it decreased with it at $n = 1000$ rpm. This could be due to the vibratory displacement in the cutting tool which causes dynamic instability, which is more common to occur at hole entry leading to higher hole circularities at the top than the bottom [17]. For feed rates and spindle speeds, ratio of 0.1 mm/rev (100/1000, 300/3000, 600/6000 and 900/9000), it was observed that hole circularity error at both sides improved when with higher spindle speed and feed rate. Hole circularity error ranged between 6.92 and 27.26 μm at the top and between 4.1 and 33.84 μm at the bottom.

3.2.4 Chip formation and post-machining hardness

Figure 17 shows samples of chips collected after drilling each hole under different cutting conditions. It was observed that wide range of chip thicknesses and lengths were formed, depending on the cutting conditions. The chip thickness increased with the increase of the feed rate and decreased with the increase of spindle speed. The chip length decreased with the increase of the feed rate and increased with the increase of spindle speed. Discontinuous and segmented chips were formed at spindle speeds $n = 1000$ and 3000 rpm and feed rates of $f = 100$, 300, 600 and 900 mm/min; at those cutting conditions, the chip was peeled off the workpiece and deformed before allowing sufficient time for the cutting lips to remove the material.

At $n = 6000$ and 9000 rpm and $f = 100$ mm/min and $n = 9000$ rpm and $f = 300$ mm/min, continuous chips were formed, they were very long, and tended to curl around the cutting tool which required manual removal; also, the formation of such chips promoted built-up edge on the cutting tools.

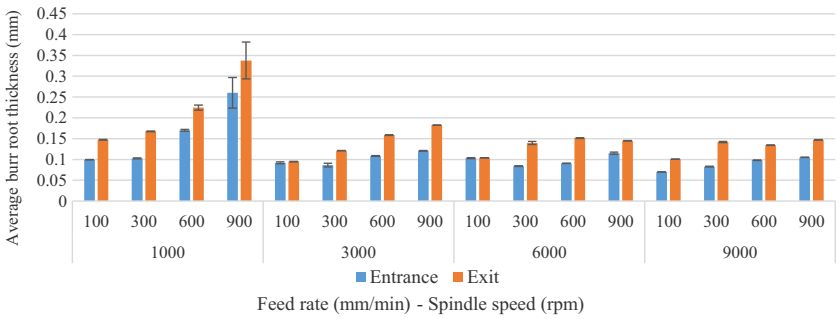

Fig. 13 Average burr root thickness at entrance and exit

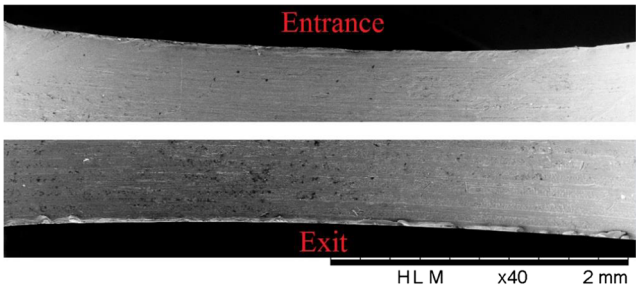

Fig. 14 SEM image showing hole edges at entrance and exit of drilled hole at $n = 1000$ rpm and $f = 100$ mm/min

It was observed that Al2024-T3 particles adhered to the cutting tool facets and cutting edges as shown in Fig. 19; the formation of built-up edges is generally undesirable [42]. Segmented chip formed at $n = 3000$ rpm and $f = 900$ mm/min. Lamerallar chips which are a type of continuous chip formation were formed at $n = 9000$ rpm and $f = 600$ mm/min. The change of chip length and thickness could be due to the increase in workpiece ductility as machining temperatures rise with spindle speed.

Figure 18 shows the post-machining microhardness at the top and bottom surfaces for each drilled hole. The increase in hardness can lead to excessive tool wear and brittleness of workpiece material which makes it more vulnerable to damage in applications was impact and fatigue are present. The hardness increased at both sides after drilling the holes; the hardness ranged between 155 and 172 HV, which is 13–25.5 % increase from its normal hardness value of 137 HV. Results indicate that it increased with spindle speed and feed rate. Also, the difference in microhardness at entrance and exit side was small with the exception of few drilled holes.

3.2.5 Hole images under optical microscopy

Figures 19 and 20 show the state of drilled holes of the first trial under different cutting conditions at entrance and exit sides, respectively. Visually inspecting the hole and using an optical microscope, it was observed that the hole surface quality was better at the entrance than at the exit side. In addition, the hole quality at entrance decreased with feed rate; best hole quality was achieved at $n = 3000$ and 6000 rpm and $f = 100$ mm/min. At those cutting parameters, the hole edge was uniform with very little burr and discontinuities compared to other holes. At exit side, the hole surface quality decreased with feed rate as well, and generally, hole surface quality was better at high spindle speeds and low feed rates.

3.2.6 Post-machining tool inspection

Figure 21 shows the condition of one of the cutting tools after drilling; inspecting the tool under microscope showed that there was high level of BUE on the cutting edges of the drill. This indicates that interaction between the cutting tool and chip of the workpiece undergoes severe friction, which caused it to weld on several regions on the cutting tool. It can also be noticed that the BUE continued to spread along the cutting edges away from the chisel edge; adhesion was also found on the chisel edge, the flanks and the crater of the drill; and the Al2024-T3 chips melted and were deposited creating a thin layer on the cutting tool surface, which could have an impact on the surface finish and reduce hole size accuracy. The use of high spindle speeds and feed rates might be the cause of BUE and adhesions on the cutting tools; thus, it is always recommended to avoid excessive feed or speeds in machining.

3.2.7 Post-machining tool inspection

Figure 22 shows the status of drilled hole under scanning electron microscopy. The scanning electron microscopy of the borehole surfaces showed that surface quality decreased with the increase of the spindle speed and feed rate. This could be due to the rise in cutting temperatures with the increase of spindle speed and increase of deformations with the increase of the feed rate. In addition, aluminium alloys have a strong alloying tendency and chemical reactivity with materials in the cutting tools at tool-operating temperatures.

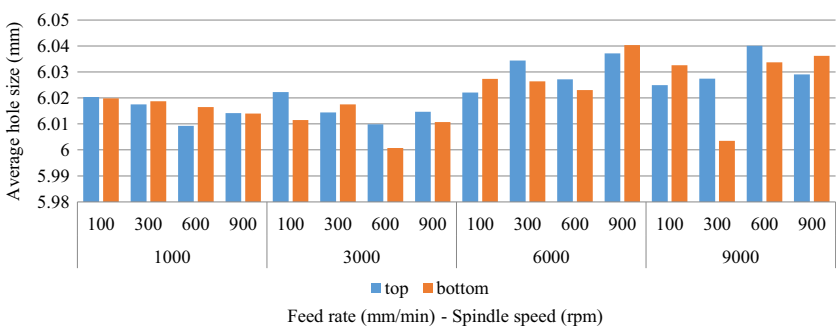

Fig. 15 Average hole size at top and bottom

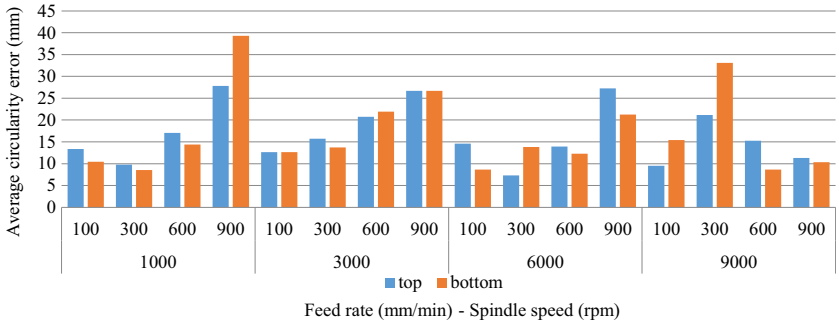

Fig. 16 Average hole circularity error at top and bottom

Smearing was observed in all drilled holes as shown in Fig. 23. The smearing increased with the increase of spindle speed and feed rate. This could be due to the increase in cutting temperatures and feed force, which increases the flowing and deformations in Al2024-T3 surface during the machining process. No visible cracks were found on the surface under all cutting conditions. However, drilling at a spindle speed of $n = 1000$ rpm and feed rates of $f = 600$ and 900 mm/min showed severe deformations within the hole walls and some chipping as shown in Fig. 24, which indicates that those cutting parameters are not suitable for drilling Al2024-T3 alloy. It was also observed that the feed marks and deformations were less on the lower part of the hole (above the hole exit) rather than the upper part (below the hole entry). This could be due to the increased ductility and flow of the material with depth due to the increase in cutting temperatures, which improves the cutting process and give better surface finish.

4 Finite element model

4.1 Material model

The FE model used to simulate the cutting mechanism in Al2024-T3 consisted of four distinct steps: (1) linear elastic behaviour governed by linear stress–strain relationship, (2) plastic behaviour using Johnson-Cook plasticity model (plastic yielding with strain hardening), (3) damage initiation using Johnson-Cook damage initiation criteria and equivalent

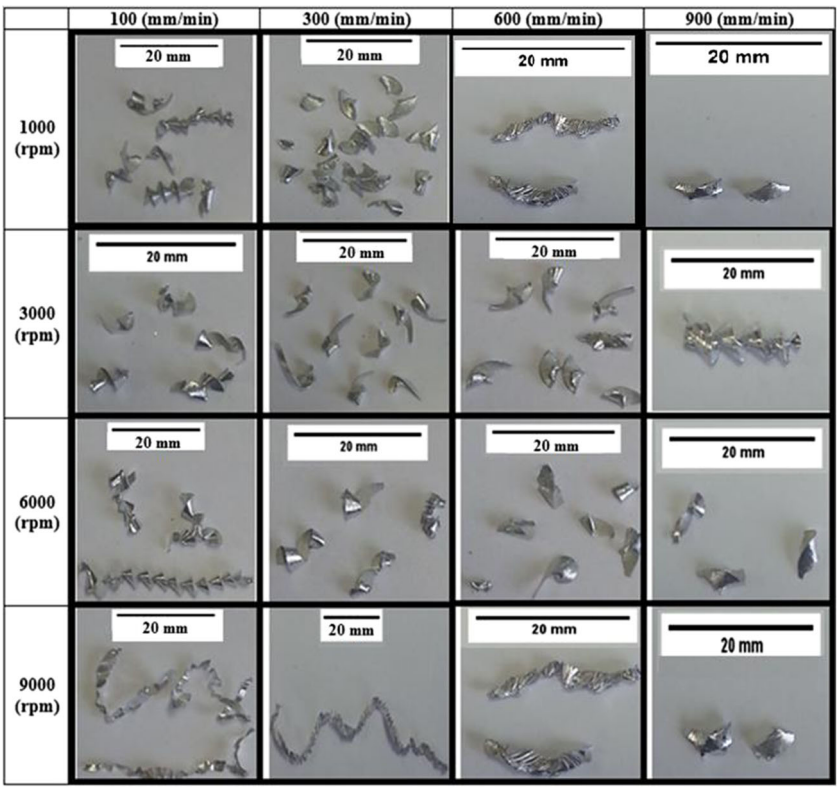

Fig. 17 Chip formation under different cutting conditions

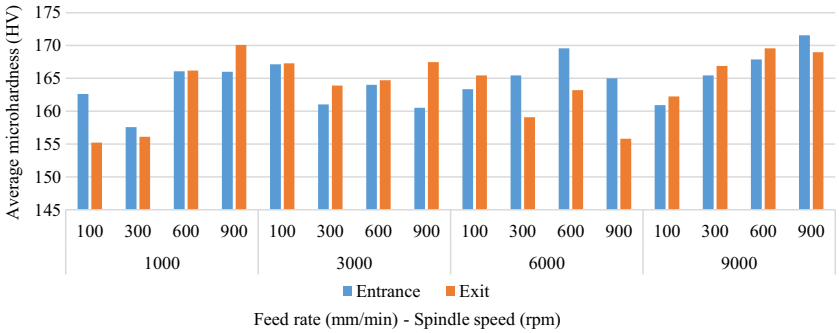

Fig. 18 Average post-machining microhardness at entrance and exit sides

plastic strain at the onset of damage, and (4) removing the element of the mesh completely upon reaching maximum degradation [43].

4.1.1 Linear elastic response

The linear stress–strain relationship is governed by $\sigma = E.\varepsilon$. Table 5 depicts some of the mechanical properties of Al2024-T3 alloy.

4.1.2 Hardening

The Johnson-Cook (JC) plasticity model was used to simulate the plastic hardening of the material. The JC model is suitable for materials which possess a linear elastic behaviour and with applications where high strain rate deformations are expected such as in machining and impact applications. The JC model is a type of Mises plasticity model which uses strain hardening and rate dependence; the model is defined with strain rate dependence as shown below.

$$\sigma = \left[A + B\left(\varepsilon^{pl}\right)^{n}\right]\left[1 + Cln\left(\frac{\dot{\varepsilon}^{pl}}{\dot{\varepsilon}_0}\right)\right]\left(1 - \left(\frac{T - T_r}{T_m - T_r}\right)^{m}\right) \quad (1)$$

where A, B, C, n and m are the material constants which were obtained by torsion tests; the constants which are provided in Table 4 were taken from previous studies on Al2024-T3 [44]. A corresponds to the initial yield stress, B is the hardening modulus, C is a dimensionless strain rate dependency coefficient, and n and m are the power exponents of the strain work-hardening and thermal-softening coefficients, respectively. ε^{pl} is the plastic strain, $\frac{\dot{\varepsilon}}{\dot{\varepsilon}_0}$ is the dimensionless plastic strain rate, ε^{pl} and ε_0 are equivalent plastic strain rate and the reference

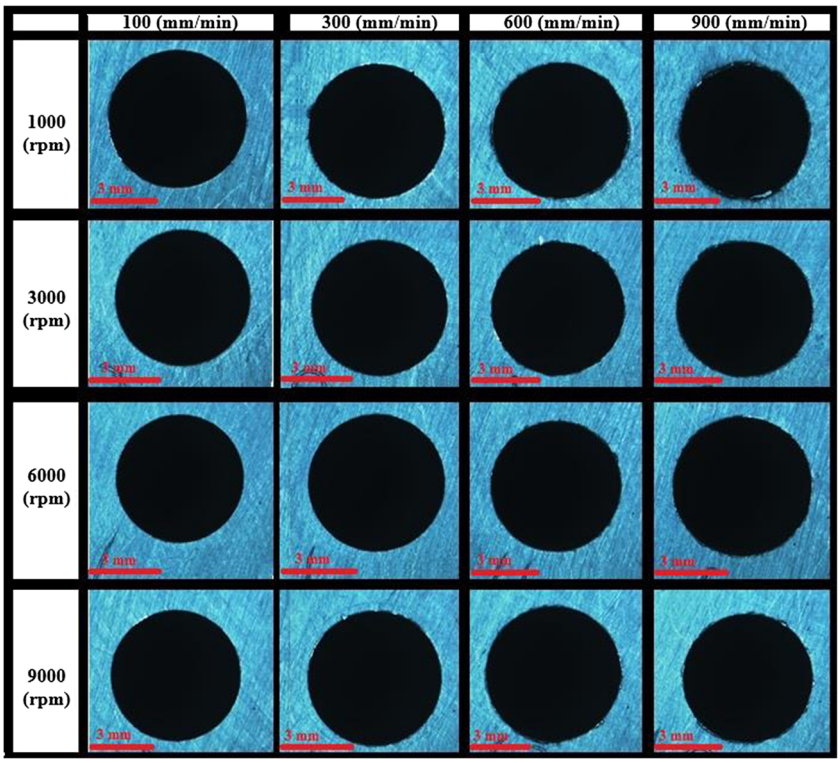

Fig. 19 Topside of drilled holes

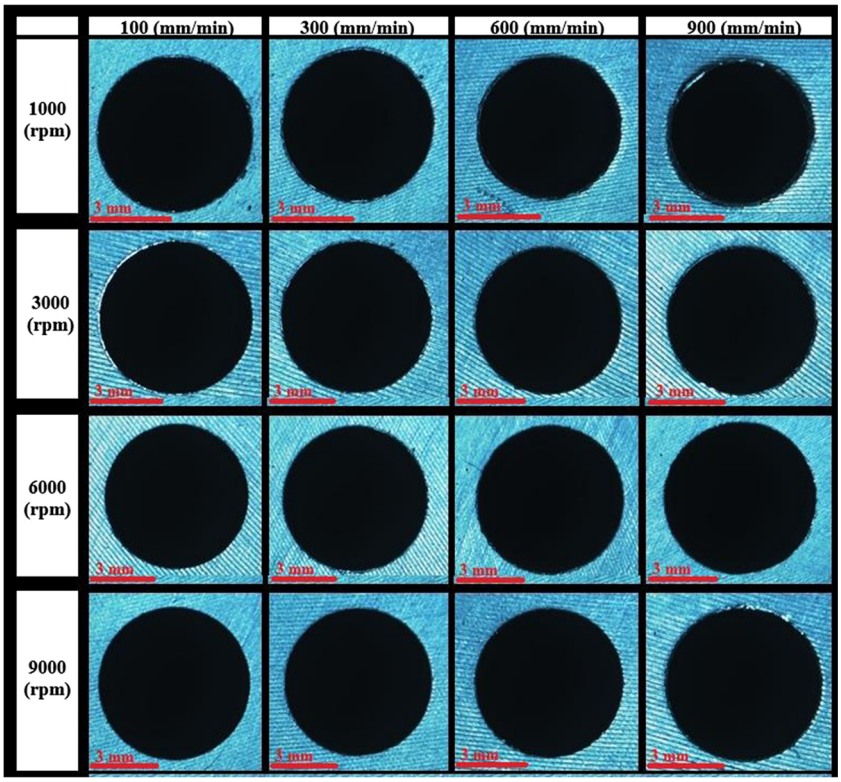

Fig. 20 Bottom side of the drilled holes

strain rate, respectively. T, T_r and T_m are the current temperature, room temperature and melting temperature of the material, respectively. The first term in the equation represents the strain hardening in the elastic plastic region, the second term represents the flow stress of the material viscosity when the material is subjected to high strain rates and the final term is related to material softening with temperature.

4.2 Modelling damage

Figure 25 shows the stress–strain diagram for the undamaged response to the complete failure and element deletion. Point 1–2 represents the undamaged material response (elastic behaviour) where the linear stress–strain relationship applies, point 2 is the yield point known as the elastic limit and point 2–3 is the plastic region at which strain hardening occurs and the material undergoes a plastic behaviour. Point 3 (ultimate yield strength) is the failure point where the onset of material damage initiation begins; after this point, the stress–strain response is governed by the evolution of stiffness degradation 3–4–5, where 3–4 represents the necking region which is part of damage evolution.

4.2.1 Damage initiation

Johnson and Cook [45] developed a model for materials that can relate the effect of strains, strain rates and temperatures on the flow stress of the ductile metals when they are subjected to high strains, strain rates and temperatures; they obtained the model constants using torsion, static tensile and dynamic Hopkinson bar tests over a wide range of strain rates and temperatures. The Johnson-Cook ductile damage criteria were

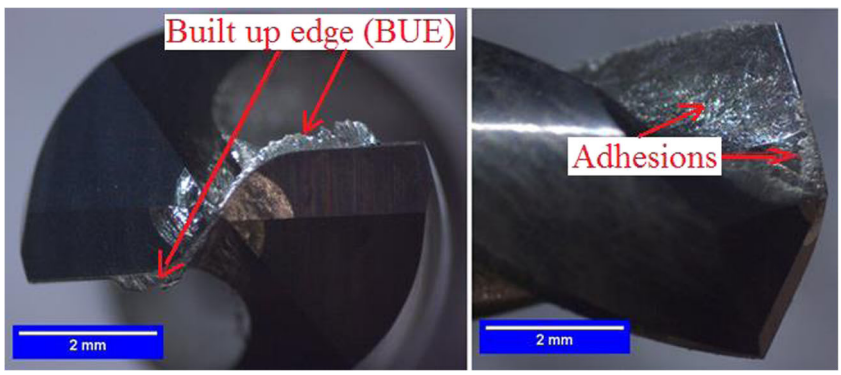

Fig. 21 Built-up edge and adhesion in the cutting tool

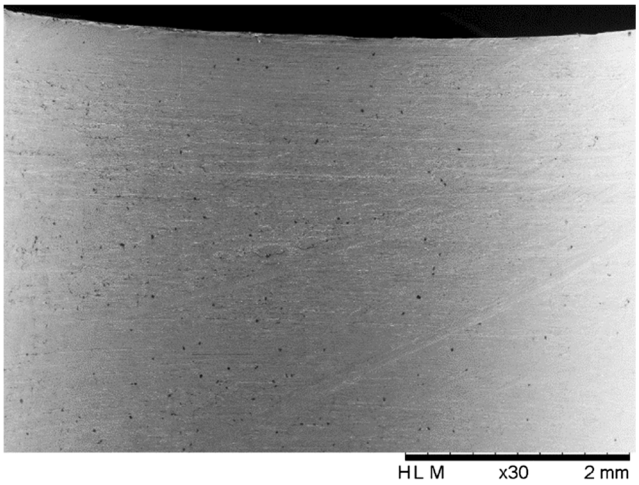

Fig. 22 Hole surface condition under SEM microscopy

used to simulate the damage initiation in Al2024-T3; the model requires the definition of five failure parameters named d_1, d_2, d_3, d_4 and d_5. The fracture occurs when $D = 0$, where D is the overall damage variable which corresponds to element removal from the workpiece when the material stiffness is fully degraded; the general expression represents the equivalent plastic strain at the onset of damage $\bar{\varepsilon}_D^{pl}$ in the following equation:

$$\bar{\varepsilon}_D^{pl} = [d_1 + d_2\exp(-d_3\eta)]^*[1 + d_4\ln(\frac{\dot{\bar{\varepsilon}}^{pl}}{\varepsilon 0})] \left(1 + d_5\left(\frac{T-T_r}{T_m-T_r}\right)^m\right) \quad (2)$$

where η is the stress triaxiality $\left(\eta = \frac{-P}{q}\right)$, P is the pressure stress and q is the Mises equivalent stress. This means that the model assumes that the equivalent plastic strain at the

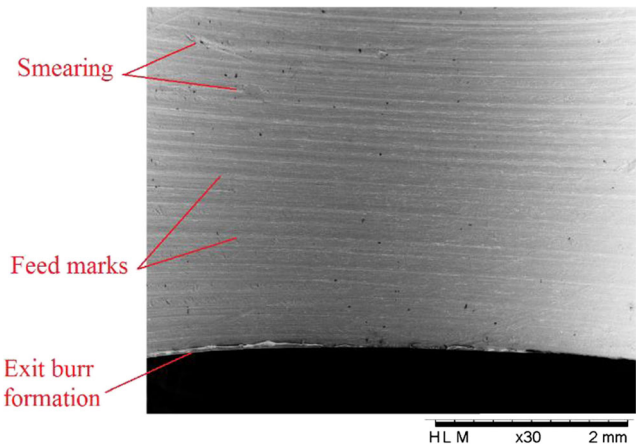

Fig. 23 Hole surface condition under SEM microscopy ($n = 1000$ rpm, $f = 100$ mm/min)

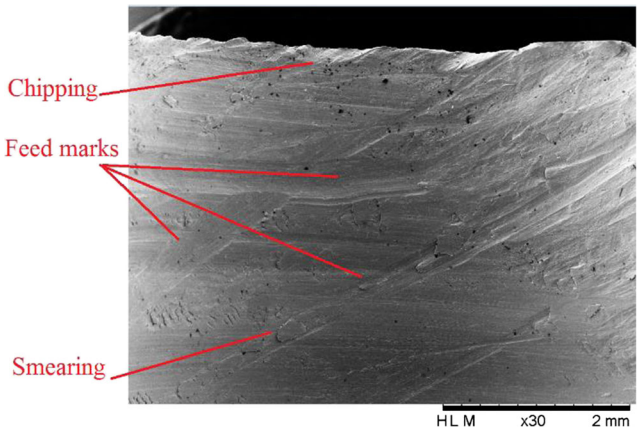

Fig. 24 Poor hole surface condition under SEM microscopy ($n = 1000$ rpm, $f = 600$ mm/min)

onset of damage $\bar{\varepsilon}_D^{pl}$ is a function of stress triaxiality and strain rate $\bar{\varepsilon}_D^{pl}(\eta, \dot{\bar{\varepsilon}}^{pl})$ [43]. The Johnson-Cook constitutive material model and damage model parameters d_1–d_5 of Al2024-T3 alloy are given in Table 6.

4.2.2 Damage evolution and element removal

When metal undergoes damage, its stress–strain relationship no longer accurately represents the material's behaviour and leads to a strong mesh dependency based on strain localisation, such that the energy dissipated decreases as the mesh size decreases [43]. Hillerborg's fracture energy criterion was used to reduce mesh dependency [43]. Hillerborg defined the energy required to open a unit area of crack, G_f, as a material parameter. With this approach, the softening response after damage initiation is characterised by a stress–displacement response rather than a stress–strain response [43]. The fracture energy is then given in Eq. (3).

$$G_f = \int_{\bar{\varepsilon}_0^{pl}}^{\bar{\varepsilon}_f^{pl}} L\sigma_y \bar{\varepsilon}^{pl} = \int_0^{\bar{u}_f^{pl}} \sigma_y \bar{u}^{pl} \quad (3)$$

This expression introduces the definition of the equivalent plastic displacement $\bar{u}^{pl}$, as the fracture work conjugate of the yield stress after the onset of damage (work per unit area of the crack). Before damage initiation, $\left(\bar{u}^{pl} = 0\right)$, and after damage initiation, $\left(\bar{u}^{pl} = L\bar{\varepsilon}^{pl}\right)$, where L is the characteristic

Table 5 Mechanical properties of Al2024-T3 used in FE simulations of drilling [44]

Density, ρ (kg/m^3)	Elastic modulus, E (GPa)	Poisson's ratio, ν	Melting temperature (°C)
2780	73.1	0.33	502

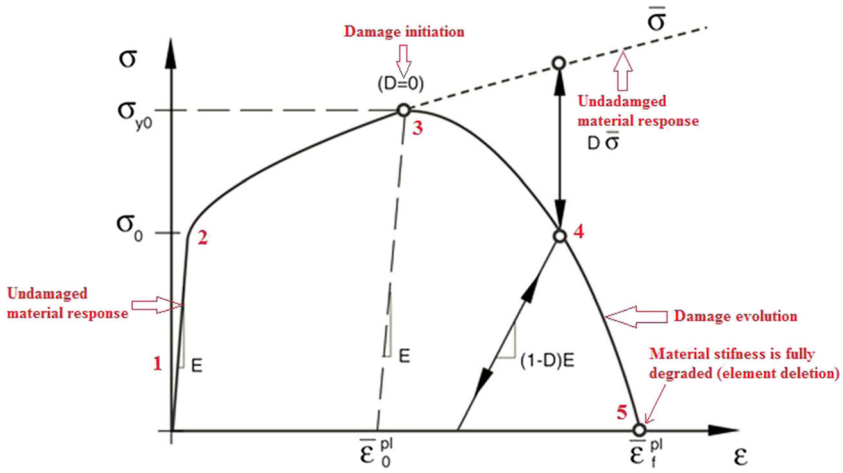

Fig. 25 Stress–strain diagram [43]

length of the element [43]. The definition of the characteristic length depends on the element topology; therefore, to avoid any mesh sensitivity in the model, the aspect ratios of the workpiece elements were kept close to unity.

The damage evolution law can be specified in terms of equivalent plastic displacement $\overline{u}^{pl}$ or in terms of fracture energy dissipation G_f. Both of these options take into account the characteristic length of the element to alleviate mesh dependency of the results [43]. The evolution of the damage variable with the relative plastic displacement is used in its linear form. It assumes a linear evolution of the damage variable with effective plastic displacement as shown in Fig. 26. The damage variable increase according to the following equation:

$$\dot{d} = \frac{L\dot{\overline{\varepsilon}}^{pl}}{\overline{u}_f^{pl}} = \frac{\dot{\overline{u}}^{pl}}{\overline{u}_f^{pl}} \tag{4}$$

This ensures that when the effective plastic displacement reaches the value $\bar{u}_{pl} = \bar{u}_{pl}^{f}$, the material stiffness will be fully degraded when $D = 1$. The linear damage evolution law defines a truly linear stress–strain softening response only if the effective response of the material is perfectly plastic (constant yield stress) after damage initiation [43] as shown in Fig. 26. As shown previously in Table 6, the fifth failure parameter d_5 is equal to zero in Al2024-T3 material, which means that there is no temperature effect on the damage initiation during the drilling process [46].

Table 6 Johnson-Cook constitutive material and damage model parameters for Al2024-T3 [45]

A (MPa)	*B* (MPa)	*C*	*n*	*m*	d_1	d_2	d_3	d_4	d_5
265	426	0.018	0.34	1	0.13	0.13	−1.5	0.011	0

Finally, the element is removed from the mesh upon reaching maximum degradation (D_{max}) using Eq. (5). The element is removed from the mesh if D=D_{max}, and no further damage are accumulated at an integration point once D reaches maximum degradation.

$$\sigma = (1-D)\overline{\sigma} \tag{5}$$

4.3 Setup of FE model

The dimensions of the workpiece used in FE model were 15 × 15 × 7.13 mm; the workpiece was fixed at all of its vertical faces and was not allowed to have any displacement in all global directions ($U_1 = U_2 = U_3$). The workpiece was partitioned at its centre by a 9-mm circle through its thickness; also, the cutting tool CAD model provided from OSG was imported to Abaqus as shown in Fig. 27. The motion of the cutting tool was restricted in X and Y global coordinates and was only allowed to translate and rotate about its Z axis, which represents the rotation (spindle speed) and translation (feed rate).

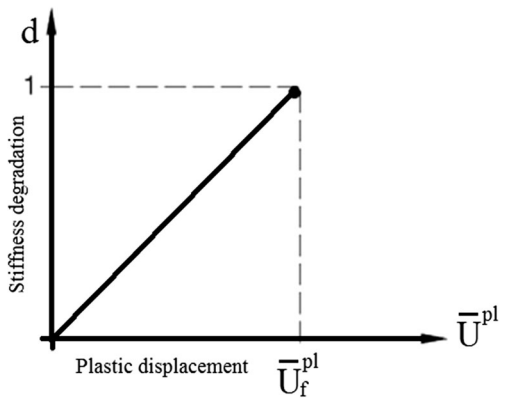

Fig. 26 The linear damage evolution law [43]

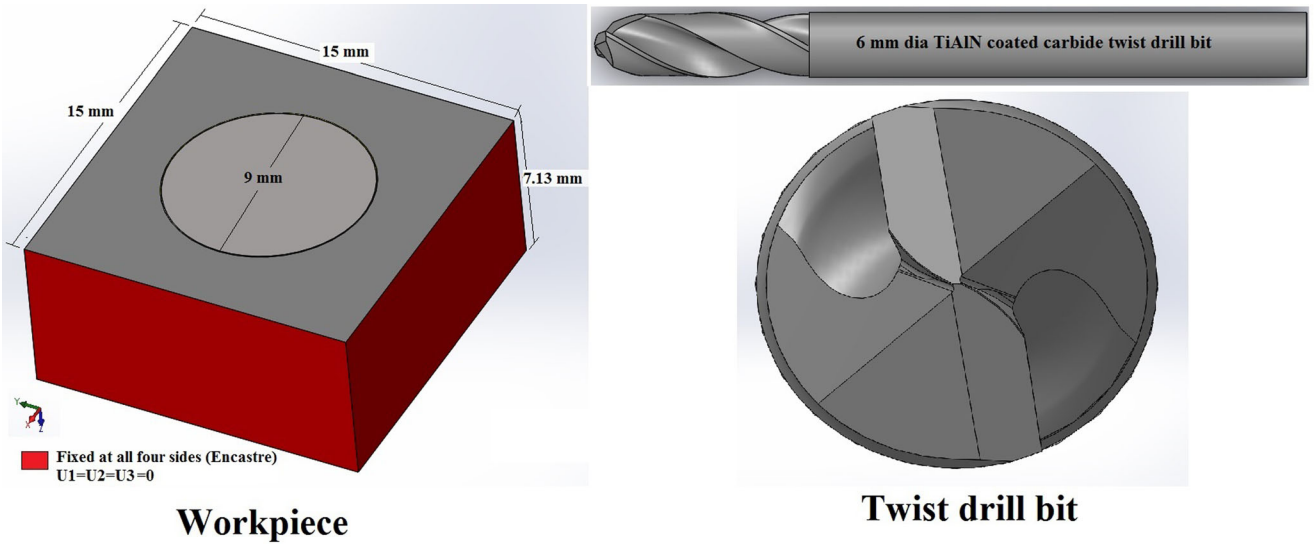

Fig. 27 Workpiece and cutting tool CAD models

4.3.1 Mesh study

Several meshing techniques and partitions were tested to validate their influence on the accuracy of the results; this allowed for mesh density optimisation, such that fine mesh was applied at the centre where drilling will take place as shown in Fig. 28, whilst coarser mesh was applied outside the circle area; this helped in reducing computational time considerably. Also, it was found that it can estimate the torque more accurately. The workpiece was modelled using solid elements available in Abaqus/Explicit. The Johnson-Cook plasticity model can be used with any elements that have displacement degrees of freedom, and thus, one integration element CD8R3 was used for the Al2024-T3 workpiece.

To further enhance the robustness of the model and its results, a vigorous mesh sensitivity study was conducted to produce results with an acceptable level of accuracy, which does not require large amounts of computational costs and time and could accurately predict cutting forces. The sensitivity study involved changing the mesh density through the thickness and within the hole vicinity. Therefore, all results shown here are based on optimised mesh analysis. Two different mesh sizes were introduced at different regions in the workpiece. A planar mesh size of 0.1885 × 0.1885 mm (in the 1–2 plane) was used for meshing the circular area at the centre of the workpiece as shown in Fig. 28. A coarser mesh of 1 × 1 mm was used in areas away from the zone of interest which were outside the circular area. The influence of mesh density through

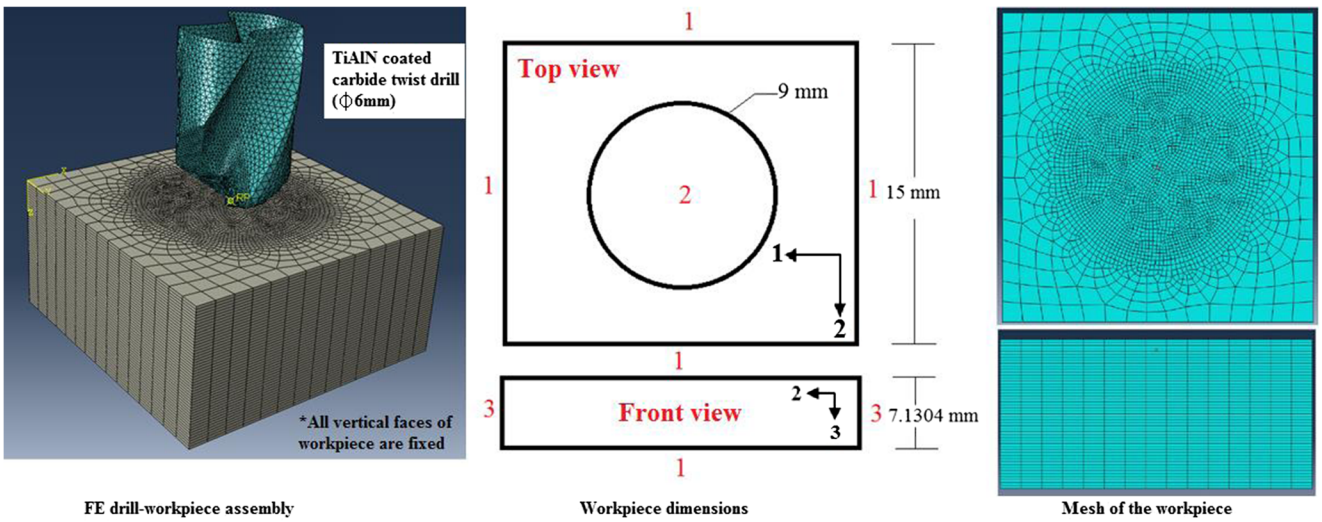

Fig. 28 Finite element model of drill and workpiece assembly

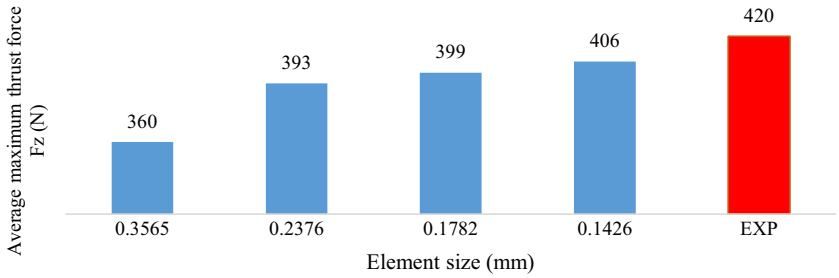

Fig. 29 Mesh convergence study through thickness

thickness was also taken into account. A planar mesh size of 0.1426 × 0.1426 mm (in the 2–3 plane) was used. Further reduction of mesh size resulted in only minor improvement in cutting forces of around 1 % but increased computational time considerably. The mesh sensitivity analysis through thickness on thrust force was shown in Fig. 29.

In order to avoid negative volume problems when the elements are deformed, enhanced hourglassing option is used to prevent hourglass deformations [43]. The distortion control was used to prevent solid elements from inverting or distorting excessively during the drilling process, which could lead to difficulties in numerical convergence. The maximum degradation option available in element control was used with progressive damage behaviour; this parameter also determines the amount of residual stiffness that will be retained by elements during the drilling process, and a default value of 0.99 was used. The effective plastic displacement-based damage criterion was chosen for damage evolution. In this case, the effective plastic displacement at failure is specified $\overline{u}_f^{pl} = 1.8e{-}5$ m

Due to the nature of the explicit solver, existence of few smaller meshed elements in the workpiece can influence the stable time increment for the whole model. In this case, the minimum stable time increment was found to be in the order of $1\,e^{-9}$ s; this would require large computational time and memory costs (more than 3,000,000 time increments for a full run). Therefore, mass scaling was applied using a fixed mass scaling factor = 1000 to artificially increase the mass of the workpiece which contained the elements with most critical stable time increment.

The cutting tool was modelled as a discrete rigid; its deformation is not accounted in the simulation process. In addition, a small part of the total drill is used in the FE models (see Fig. 28). This reduces the required computational time considerably. R3D3 rigid triangular facet elements are used to mesh the cutting tool with a total number of elements equal to 13,663. The refined mesh was applied on the cutting edges and the two facets of the drill where interaction will take place with the workpiece material.

4.3.2 Contact, loading and boundary conditions

The workpiece and cutting tool contact modelling was defined using the general contact algorithm available in Abaqus/Explicit. The friction between the cutting tool and workpiece surfaces was defined using the simple Coulomb friction model, which relates the maximum allowable frictional stress across an interface to the contact pressure between the contacting bodies due to the rotational movement of the cutting tool. The Coulomb friction has been widely used in previous machining simulations and is also well documented for machining aluminium alloys, including Al2024-T3 alloy with various cutting tools and machining operations. Literature reports that TiAlN tool coating can have a coefficient of friction between 0.6 and 1 against aluminium (Al_2O_3) under dry conditions [47], whilst other sources indicate that TiAlN coating could have a coefficient of friction as low as 0.3 [48] and as high as 0.7 [49] against various materials. Based on the AST-G99-5 standard, the TiAlN coating has a coefficient of friction which ranges between 0.6 and 0.8 [50]. Oberg [51] reported that it had a fixed value of 0.6. Jin [52] used a constant

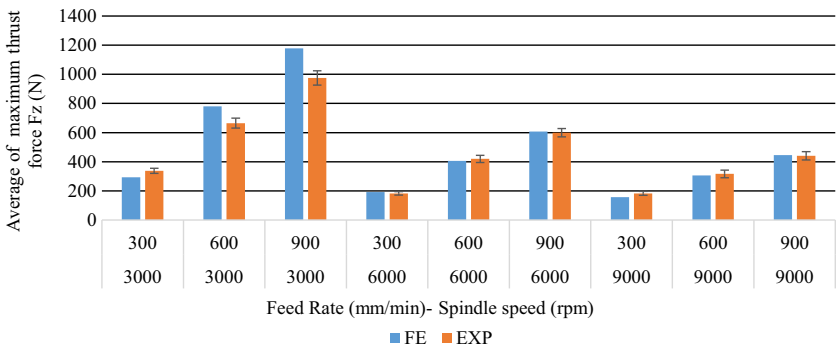

Fig. 30 Comparison between experimental and FE results of average maximum thrust force at different spindle speeds and feed rates

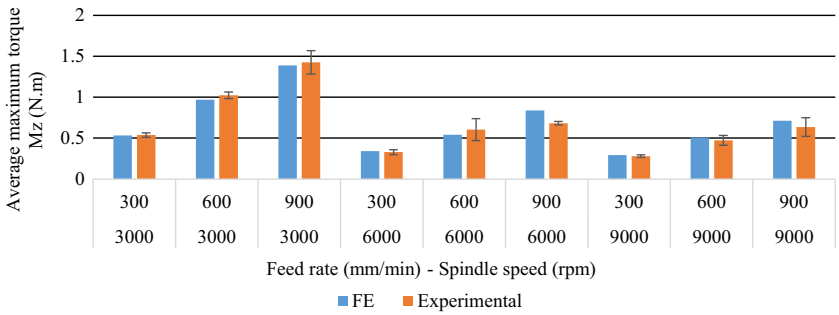

Fig. 31 Comparison between experimental and FE results of average maximum torque at different spindle speeds and feed

coefficient of friction of 0.3 when machining Al2024-T3, whilst Seshadri et al. [53] used a coefficient of friction $\mu = 0.43$ in the orthogonal cutting modelling of Al2024-T3 alloy. However, Yang et al. [54] used a value of 0.7 for microend milling of Al2024-T3 alloy. Therefore, the coefficient of friction of 0.6 was selected after a vigorous mesh study, where it was varied from 0.4 to 0.8 used in previous studies. This value also gave FE results close to those tested at cutting parameters of 6000 rpm and 600 mm/min used in the mesh convergence study.

5 FE results

Figures 30 and 31 show a comparison of the average maximum thrust force and torque between experiment results and FE simulation. In order to get better consistency values from the FE model to be compared with experimental data, a medium feed rate of $f = 600$ mm/min and spindle speed of $n = 6000$ rpm were used (0.1 mm/rev) for mesh optimisation study; then, it was applied to all other cutting parameters used in FE models. All of the optimisation studies were carried out using this combination of cutting parameters and were used later to predict the thrust force and torque for all other cutting parameters used in the experimental work.

The FE model slightly overestimates/underestimates the thrust force and torque; the discrepancy with experimental results ranged between 1 and 20.8 %. For example, the experimental thrust force and torque at $n = 9000$ rpm and $f = 900$ mm/min were found to be 441 ± 28.6 N and 0.634 ± 0.114 Nm on average, whilst FE model estimated thrust force to be 445 N and torque to be 0.7136. This indicates that the FE models are capable of predicting the cutting forces accurately. It was also observed that the inaccuracy between FE and experimental results increased with feed rate. Figures 32 and 33 show a comparison between simulation and experimental results for the thrust force profile at $n = 6000$ rpm and $f = 900$ mm/min and for torque profile at $n = 3000$ rpm and $f = 900$ mm/min.

Several factors can improve the accuracy of the current FE model, such as the use of a more realistic friction models which could account for different cutting parameters and their effect on contact stresses and temperatures; this could better represent the friction characteristics between the tool-workpiece and chip-tool interface. The thermal effects are not taken into account. Also, the tool was modelled as a rigid body; a more realistic model of the cutting tool with deformation and wear could improve the results further. In addition, the type of elements used to influence the results, even though using reduced integration elements, helps to reduce the simulation time, but it could have a significant effect on the accuracy of the integration used in stiffness matrix formulation and the way that the elements will deform; using them will reduce the stiffness of the element compared to full integration.

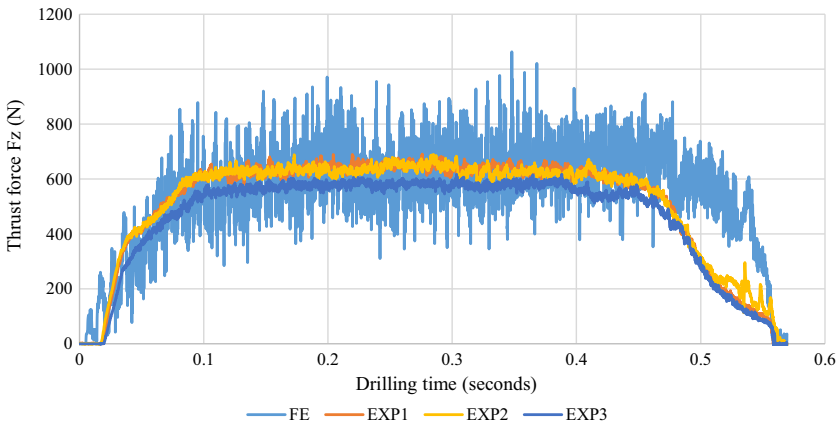

Fig. 32 Comparison of simulation results vs experiment for thrust force profile at $n = 6000$ rpm and $f = 900$ mm/min

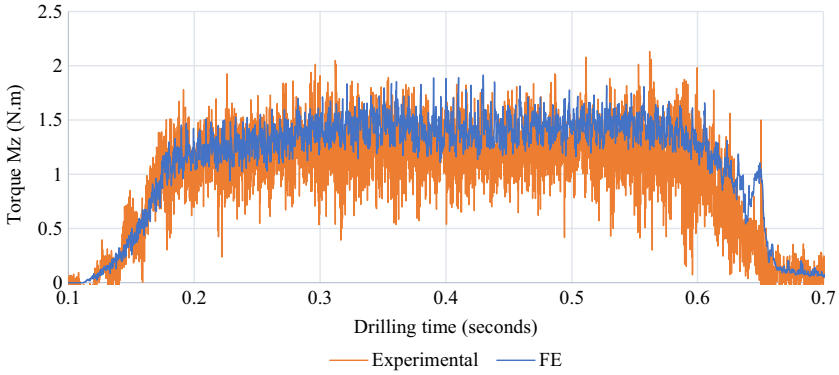

Fig. 33 Comparison of simulation results vs experiment for torque profile at $n = 3000$ rpm and $f = 900$ mm/min

6 Conclusions

In this paper, the effect of machining parameters on cutting forces in the drilling of the Al2024-T3 aluminium alloy was investigated both experimentally and numerically. Hole quality was evaluated in terms of its size and circularity error, burr formation and chip characteristics. The 3D FE model of drilling in Al2024-T3 was developed using Abaqus/Explicit, which accounts for plastic deformation, damage initiation followed by damage evolution and element deletion. The following conclusions can be drawn from this study.

- A 3D finite element model was developed using Abaqus/Explicit to simulate the drilling process of Al2024-T3 aluminium alloy, the cutting forces predicted by the FE models were in good agreement with experimental results, the variation amongst them ranged between 1 and 20.8 % and the discrepancy between experimental and FE results increased with feed rate.
- The average surface roughness R_a increased with the increase of spindle speed and the feed rate, and the influence of feed rate on surface roughness was greater than the spindle speed.
- Burr height and burr root thickness increased with the increase of feed rate, whilst spindle speed had different influence depending on its level. The spindle speed was more dominant than the feed rate on burr thickness, whilst feed rate was more dominant on burr height.
- Oversized holes were produced in all holes; the hole oversize increased with depth. Drilling at high spindle speeds and low feed rates can considerably influence the hole size. The increase ranged between 0.01 and 0.66 % of nominal hole size.
- Feed rate and spindle speed had a different influence on circularity error depending on the combination of cutting parameters used. The circularity error at top and bottom increased with the increase of feed rate when drilling at $n = 3000$ and 6000 rpm, whilst it decreased with feed rate at $n = 1000$ and 9000 rpm.
- An increase in workpiece microhardness was observed in all holes which ranged from 13 to 25.5 % from its normal hardness value of ~137 HV.
- Microhardness increased with spindle speed and feed rate, and the variation of hardness between entrance and exit sides was negligible with the exception of few drilled holes.
- Various chip lengths and thickness were formed at different cutting parameters. The formation of long chips was observed at high spindle speeds and low feed rates; such chips are undesirable as they curl around the cutting tool and could deteriorate the machined hole quality.

Acknowledgments The authors would like to thank the Advanced Manufacturing Research Centre (AMRC with Boeing) in Sheffield for providing the access to their machining facilities. The authors also thank Mr. Jacob Hawxwell (Sandvik Coromant-Sheffield) for his help with CMM measurements. Support from OSG regarding the provision of CAD model is also acknowledged. Mr. Khaled Giasin would like to thank the Department of Mechanical Engineering at the University of Sheffield for the awarded Ph.D. scholarship.

References

1. Farid AA, Sharif S, Idris MH (2011) Chip morphology study in high speed drilling of Al–Si alloy. Int J Adv Manuf Technol 57(5–8):555–564
2. Carter Ralph W, Steven Johnson W, Toivonen P, Makeev A, Newman JC Jr (2006) Effect of various aircraft production drilling procedures on hole quality. Int J Fatigue 28(8):943–950
3. Shop MM (2010) Presetting process cuts scrap, rework. Modern machine shop, Modern machine shop
4. Hashimura M, Chang Y, Dornfeld D (1999) Analysis of burr formation mechanism in orthogonal cutting. J Manuf Sci Eng 121(1): 1–7
5. Nouari M, List G, Girot F, Coupard D (2003) Experimental analysis and optimisation of tool wear in dry machining of aluminium alloys. Wear 255(7):1359–1368
6. Fang N, Wu Q (2005) The effects of chamfered and honed tool edge geometry in machining of three aluminum alloys. Int J Mach Tools Manuf 45(10):1178–1187

7. Shareef I, Natarajan M, Ajayi OO (2005) Dry machinability of aluminum alloys. In: World tribology congress III. American Society of Mechanical Engineers pp 831–832
8. Dhanorker A, Özel TR (2006) An experimental and modeling study on meso/micro end milling process. In: ASME 2006 International Manufacturing Science and Engineering Conference. American Society of Mechanical Engineers, pp 1071–1079
9. Chern G-L (2006) Experimental observation and analysis of burr formation mechanisms in face milling of aluminum alloys. Int J Mach Tools Manuf 46(12–13):1517–1525
10. Subbiah S, Melkote SN (2008) Effect of finite edge radius on ductile fracture ahead of the cutting tool edge in micro-cutting of Al2024-T3. Mater Sci Eng A 474(1–2):283–300
11. Adnan AS, Subbiah S (2010) Experimental investigation of transverse vibration-assisted orthogonal cutting of AL-2024. Int J Mach Tools Manuf 50(3):294–302
12. Haddag B, Atlati S, Nouari M, Barlier C, Zenasni M (2012) Analysis of the cutting parameters influence during machining aluminium alloy A2024-T351 with uncoated carbide inserts. Eng Trans 60(1):31–39
13. Mohamed SB, Mohamad WNF, Minhat M, Kasim MS, Ibrahim Z, Musanih MR (2015) Machining parameters optimization for trimming operation in a milling machine using two level factorial design. In: Applied mechanics and materials. Trans Tech Publications pp 105–110
14. Çakır A, Yağmur S, Kavak N, Küçüktürk G, Şeker U (2015) The effect of minimum quantity lubrication under different parameters in the turning of AA7075 and AA2024 aluminium alloys. Int J Adv Manuf Technol 1–7
15. Nouari M, List G, Girot F, Géhin D (2005) Effect of machining parameters and coating on wear mechanisms in dry drilling of aluminium alloys. Int J Mach Tools Manuf 45(12–13):1436–1442
16. Kurt M, Bagci E, Kaynak Y (2009) Application of Taguchi methods in the optimization of cutting parameters for surface finish and hole diameter accuracy in dry drilling processes. Int J Adv Manuf Technol 40(5–6):458–469
17. Kurt M, Kaynak Y, Bagci E (2008) Evaluation of drilled hole quality in Al 2024 alloy. Int J Adv Manuf Technol 37(11): 1051–1060
18. Köklü U (2012) Influence of the process parameters and the mechanical properties of aluminum alloys on the burr height and the surface roughness in dry drilling. Materiali Tehnologije 46(2):103–108
19. Davoudinejad A, Ashrafi SA, Hamzah RIR, Niazi A (2012) Experimental analysis of wear mechanism and tool life in dry drilling of Al2024. In: Advanced materials research. Trans Tech Publ pp 217–221
20. Amini S, Paktinat H, Barani A, Tehran AF (2013) Vibration drilling of Al2024-T6. Mater Manuf Process 28(4):476–480
21. Mohamed Elajrami HMaFBB (2013) Effect of drilling parameters on hole quality. Int J Min Metall Mech Eng 1 (4):254–257
22. Barani A, Amini S, Paktinat H, Tehrani AF (2014) Built-up edge investigation in vibration drilling of Al2024-T6. Ultrasonics 54(5): 1300–1310
23. Abdelhafeez AM, Soo SL, Aspinwall DK, Dowson A, Arnold D (2015) Burr formation and hole quality when drilling titanium and aluminium alloys. Procedia CIRP 37:230–235
24. Barani A, Amini S, Paktinat H, Fadaei Tehrani A (2014) Built-up edge investigation in vibration drilling of Al2024-T6. Ultrasonics 54(5):1300–1310
25. Davim JP (2011) Modern machining technology: a practical guide. Elsevier
26. Ko S-L, Lee J-K (2001) Analysis of burr formation in drilling with a new-concept drill. J Mater Process Technol 113(1–3):392–398. doi: 10.1016/s0924-0136(01)00717-8
27. Dandekar C, Orady E, Mallick PK (2007) Drilling characteristics of an E-glass fabric-reinforced polypropylene composite and an aluminum alloy: a comparative study. J Manuf Sci Eng 129(6):1080–1087
28. Batzer S, Haan D, Rao P, Olson W, Sutherland J (1998) Chip morphology and hole surface texture in the drilling of cast aluminum alloys. J Mater Process Technol 79(1):72–78
29. Isbilir O, Ghassemieh E (2011) Finite element analysis of drilling of titanium alloy. Procedia Eng 10:1877–1882
30. Soo S, Aspinwall D, Dewes R (2004) 3D FE modelling of the cutting of Inconel 718. J Mater Process Technol 150(1):116–123
31. Mabrouki T, Rigal J-F (2006) A contribution to a qualitative understanding of thermo-mechanical effects during chip formation in hard turning. J Mater Process Technol 176(1):214–221
32. Chang C-S (2007) Prediction of the cutting temperatures of stainless steel with chamfered main cutting edge tools. J Mater Process Technol 190(1):332–341
33. Hortig C, Svendsen B (2007) Simulation of chip formation during high-speed cutting. J Mater Process Technol 186(1):66–76
34. Hua J, Shivpuri R (2004) Prediction of chip morphology and segmentation during the machining of titanium alloys. J Mater Process Technol 150(1):124–133
35. Jeevannavar A, Hussain R (2014) Process modelling, simulation and experimental validation for prediction of chip morphology during high speed machining of Al 2024-T3. SAS TECH J 13(1):72–80
36. Asad M, Girardin F, Mabrouki T, Rigal J-F (2008) Dry cutting study of an aluminium alloy (A2024-T351): a numerical and experimental approach. Int J Mater Form 1(1):499–502
37. Akram S, Jaffery SHI, Khan M, Mubashar A, Ali L A numerical investigation of effects of cutting velocity and feed rate on residual stresses in aluminum alloy Al-6061
38. Shi G, Deng X, Shet C (2002) A finite element study of the effect of friction in orthogonal metal cutting. Finite Elem Anal Des 38(9): 863–883
39. Hazarika M, Dixit US (2014) Setup planning for machining. Springer International Publishing
40. Shanmughasundaram P, Subramanian R (2014) Study of parametric optimization of burr formation in step drilling of eutectic Al–Si alloy–Gr composites. J Mater Res Technol 3(2):150–157
41. Stephenson DA, Agapiou JS (2005) Metal cutting theory and practice, vol 68. CRC press
42. Toenshoff HK, Denkena B (2013) Basics of cutting and abrasive processes. Springer
43. Version A 6.13 Documentation (Abaqus), 2013. Abaqus user's guide
44. Lesuer DR (1999) Experimental investigations of material models for Ti-6A1-4V and 2024-T3 University of California, Lawrence Livermore National Laboratory, Livermore
45. Johnson GR, Cook WH (1983) A constitutive model and data for metals subjected to large strains, high strain rates and high temperatures. In: Proceedings of the 7th International Symposium on Ballistics. The Hague, Netherlands: International Ballistics Committee, pp 541–547
46. Mabrouki T, Girardin F, Asad M, Rigal J-F (2008) Numerical and experimental study of dry cutting for an aeronautic aluminium alloy (A2024-T351). Int J Mach Tools Manuf 48(11):1187–1197
47. Straffelini G (2015) Friction and wear: methodologies for design and control. Springer International Publishing

48. Cheng K (2008) Machining dynamics: fundamentals, applications and practices. Springer Science & Business Media
49. Rao PN (2013) Manufacturing technology: metal cutting and machine tools. v. 2. Tata McGraw-Hill Education
50. Qin Y (2015) Micromanufacturing engineering and technology. Elsevier Science
51. Oberg E (2012) Machinery's handbook 29th edition-full book. Industrial Press
52. Jin X (2012) Mechanics and dynamics of micro-cutting process. Ph.D, The University of British Columbia-Vancouver
53. Seshadri R, Naveen I, Srinivasan S, Viswasubrahmanyam M, VijaySekar K, Kumar MP (2013) Finite element simulation of the orthogonal machining process with Al 2024 T351 aerospace alloy. Procedia Eng 64:1454–1463
54. Yang K, Liang Y-C, Zheng K-N, Bai Q-S, Chen W-Q (2011) Tool edge radius effect on cutting temperature in micro-end-milling process. Int J Adv Manuf Technol 52(9–12):905–912